



Interaction of metal ions in high efficiency seawater hydrogen peroxide production by a carbon-based photocatalyst

Jiacheng Li^a, Hong Shi^a, Zenan Li^a, Jiaxuan Wang^a, Honglin Si^a, Fan Liao^{a,*}, Hui Huang^{a,*}, Yang Liu^{a,*}, Zhenhui Kang^{a,b,**}

^a Institute of Functional Nano & Soft Materials (FUNSOM), Jiangsu Key Laboratory for Carbon-Based Functional Materials & Devices, Soochow University, 199 Ren'ai Road, Suzhou 215123, China

^b Macao Institute of Materials Science and Engineering (MIMSE), MUST-SUDA Joint Research Center for Advanced Functional Materials, Macau University of Science and Technology, Taipa 999078, Macao

ARTICLE INFO

Keywords:

Hydrogen peroxide
Photocatalysis
Carbon-based photocatalyst
Transient photovoltage
Machine learning

ABSTRACT

Photocatalytic seawater splitting is a promising method for producing hydrogen peroxide (H₂O₂). However, the presence of metal ions usually deactivates catalysts and causes undesirable reactions, highlighting the need for deeply understanding these interactions. Herein, a carbon-based composite photocatalyst (CQM) is fabricated for photocatalytic production of H₂O₂. The metal ions strongly affect the photocatalytic activity of the CQM catalyst with order of Mg²⁺ > Al³⁺ > Ca²⁺ > K⁺, consistent with the surface effective electron concentration calculated from transient photovoltage (TPV) technology. Notably, with the presence of Mg²⁺ at 0.36 mol L⁻¹, the H₂O₂ yield is 12,812 μmol g⁻¹ h⁻¹. Under the guidance of machine learning, the H₂O₂ yield is further improved to 19,560 μmol g⁻¹ h⁻¹ by adjusting the concentration of multiple ions. Significantly, in a real seawater system, the photoproduction of H₂O₂ on CQM reaches up to a recorded value of 11306 μmol g⁻¹ h⁻¹ under visible light illumination.

1. Introduction

Photocatalysis is an effective technology to solve the environmental pollution problems, energy crisis and sustainable development challenges [1–7]. More attention should be paid to the applications of photocatalysis in actual production. However, it is still a challenge to study the photocatalytic mechanisms in the complexity of practical application systems. For example, the photocatalytic splitting of seawater, a promising and resource-preferred method [8–14], is used for the production of H₂O₂.

The mainstream process for industrial production of H₂O₂ is anthraquinone oxidation method (AQ). However, the AQ oxidation process requires a high energy input and produces a large amount of wastewater due to multiple hydrogenation and oxidation reactions [15, 16]. Another method is directly synthesis of H₂O₂ through H₂ and O₂ catalyzed by noble metal catalysts [17–19]. Unfortunately, the high cost, low H₂O₂ selectivity and explosion risk of H₂/O₂ mixture make this technology difficult to scale up to industrial applications [20,21].

Therefore, there is an urgent need for an environmentally friendly and safe process to produce H₂O₂. Solar-driven photocatalytic production of H₂O₂ is one of the most promising methods, which only requires abundant water and oxygen as raw materials and renewable sunlight as energy supply. In particular, it can produce H₂O₂ on-site and on-demand, avoiding the risk of dangerous concentrated H₂O₂ production and transportation.

It has been reported that the presence of metal ions often deactivates photocatalysts and triggers undesirable reactions [22–24], which necessitates a deeper understanding of these interactions to enhance the activity of photocatalysts.

Compared to transition metal-based semiconductor catalysts, carbon-based catalysts exhibit high stability in seawater and prevent the decomposition of H₂O₂. Efforts have been made to develop the high-efficient carbon-based catalysts for H₂O₂. For example, Zeng *et al.* demonstrated a novel strategy to enhance the photocatalytic H₂O₂ production by modifying C₃N₄ nanosheets with polyethylenimine (PEI/C₃N₄), which exhibits a H₂O₂ generation activity of 208.1 μmol g⁻¹ h⁻¹

* Corresponding authors.

** Corresponding author at: Institute of Functional Nano & Soft Materials (FUNSOM), Jiangsu Key Laboratory for Carbon-Based Functional Materials & Devices, Soochow University, 199 Ren'ai Road, Suzhou 215123, China.

E-mail addresses: fliao@suda.edu.cn (F. Liao), hhuang0618@suda.edu.cn (H. Huang), yangl@suda.edu.cn (Y. Liu), zhkang@suda.edu.cn (Z. Kang).

<https://doi.org/10.1016/j.apcatb.2023.123541>

Received 20 September 2023; Received in revised form 9 November 2023; Accepted 19 November 2023

Available online 21 November 2023

0926-3373/© 2023 Elsevier B.V. All rights reserved.

under simulated solar light irradiation [25]. Additionally, Han's group synthesized a photocatalyst based on a partially fluorinated triazine covalent organic framework (TF50-COF) that can efficiently produce H_2O_2 from water and oxygen under visible light with a yield of $1739 \mu\text{mol g}^{-1} \text{h}^{-1}$ [12]. Although researchers have proposed strategies to improve the H_2O_2 yield of carbon-based catalysts [26–28], the performance of these materials remains at the level of thousands of micromoles per hour per gram or even lower. Furthermore, most carbon-based catalysts for photocatalytic H_2O_2 synthesis are still limited by factors such as poor light absorption, band gap mismatch, low charge transfer rate, and the need for sacrificial agents [3,29].

In this paper, a new type of carbon-based photocatalyst CQM was synthesized by hydrothermal method using quercetin and methyl blue as raw materials. The effects of metal ion types and their concentrations on the H_2O_2 yields of CQM were firstly investigated by transient photovoltage (TPV) technology. According to the surface effective electron numbers (n_e) extracted from the TPV curves, the contribution of different ions to H_2O_2 yields is determined to be $\text{Mg}^{2+} > \text{Al}^{3+} > \text{Ca}^{2+} > \text{K}^+$. Then, under the guidance of machine learning (ML), the H_2O_2 yields on CQM in solution with different metal ions were predicted, which can reach a maximum of $19465 \mu\text{mol g}^{-1} \text{h}^{-1}$ while the experiment result shows that the maximum can reach $19,560 \mu\text{mol g}^{-1} \text{h}^{-1}$. The experiment result and the prediction result match well, which proves the validity of the model predictions. The feature importance ranking of metal ions from the ML model is the same as obtained by TPV. In order to further explore the mechanism of metal ions in water on the photocatalytic process, the interactions of metal ions on H_2O_2 yields with changes in types and concentrations in multi-ions systems were discussed through SHapley Additive exPlanation (SHAP) analysis. We found that the interactions between metal ions can promote the hydrogen peroxide yield in most cases. In a real seawater system, the H_2O_2 yield on CQM can reach $11306 \mu\text{mol g}^{-1} \text{h}^{-1}$, and after five cycles of testing, there was no significant decline in performance.

CQM is a low cost carbon-based photocatalyst, which shows high catalytic activity in the production of H_2O_2 in real seawater. The salts in seawater may reduce the catalyst's light absorption, decrease the electron transfer ability, change the band gap and band position, resulting in catalyst deactivation and hindering the catalyst's reaction activity and lifetime [30–32]. The photocatalytic performance in seawater is usually lower than that in pure water [33]. However, CQM catalyst can effectively use the interaction between the complex components in seawater to improve its photocatalytic production of H_2O_2 , with its yield in seawater 15 times higher than that in deionized water.

This study opens up a new way to discover the law of metal ion influence on H_2O_2 production in complex ion environments and provides platform for improving the H_2O_2 generation in seawater.

2. Experimental section

2.1. Materials

All the chemicals used in the experiment are purchased from Sino-pharm Chemical Reagent Co, Ltd. The seawater in the experiments comes from the Yellow Sea. Ultrapure water (Millipore, $\geq 18.2 \text{ M}\Omega \text{ cm}^{-1}$) was used throughout the work.

2.2. Synthesis of CQM catalyst

The CQM catalyst was synthesized with quercetin and methyl blue as raw material. 0.2 g quercetin and 0.1 g methyl blue were dispersed in a solution consisting of 5 ML of deionized water and 1 ML of ethanol. The mixed suspension was sonicated for 5 min, then transferred into a 50 ML Teflon-lined stainless-steel autoclave, and heated at 200°C for 15 h. Then, the reacted solution was centrifuged and washed three times with deionized water and the precipitate was vacuum dried at 70°C for 10 h to get CQM. Additionally, different mass ratios of quercetin and methyl

blue were designed to explore their influence on the photocatalytic performance. The ratios were set at 1: 1, 3: 2, 6: 1, 9: 1 and 12: 1, respectively.

2.3. Photocatalytic experiments

The photocatalytic performance of the catalyst was studied by a multichannel photochemical reaction system (PCX50B, Beijing Perfect light Co. Ltd, China) under visible light ($420 \text{ nm} \leq \lambda < 700 \text{ nm}$). The average irradiation intensity was 10.28 mW cm^{-2} . 10 mg sample was dispersed into a 40 ML reaction bottle containing 15 ML deionized water or seawater, and then the mixture was stirred continuously for 1 h under normal pressure or visible light. No sacrificial or ancillary catalysts were required throughout the reaction.

The photocatalytic performance and reaction mechanism of the catalyst under different conditions were probed by varying the illumination time (1, 4, 6 and 12 h), excitation wavelength of light ($\lambda = 365, 485, 595$ and 630 nm), reaction atmosphere (air, N_2 , O_2), and adding 1 mM sacrificial agents (AgNO_3 , methyl alcohol (MA), tert-butyl alcohol (TBA), benzoquinone (BQ)). The sample after each illumination was centrifuged, washed, dried, and then used for stability testing (1 h for each cycle).

To investigate the effect of different metal ions on the catalytic activity, we firstly prepared five types of ionic solutions with concentration of 4 M: KCl, NaCl, MgCl_2 , CaCl_2 , and AlCl_3 . Then, 10 mg of CQM, deionized water, and certain volume of the above ionic solutions were added to the reaction bottle. The total liquid volume in the reaction bottle should be 15 ML, and the concentration of metal ions in the reaction bottle should be equal to the concentration of metal ions in a certain group of data in Table S3. The reaction bottle containing the catalyst and metal ions was then ultrasounded to disperse the CQM evenly in the solution before exposing it to illumination. Such operations were carried out 168 times according to Table S3, and their photocatalytic H_2O_2 yields were respectively tested and recorded to train the ML models.

Potassium permanganate (KMnO_4) titration was used to determine the amount of H_2O_2 in the process of photocatalysis. First, the solution after photocatalytic reaction was filtered with $0.22 \mu\text{m}$ of filter. Then, 5 ML of the filtered liquid was extracted and titrated with 0.004 mol L^{-1} KMnO_4 until the solution did not fade within 30 s. Finally, the yield of H_2O_2 is calculated by the titrated volume of KMnO_4 .

3. Results and discussion

3.1. Characterization of CQM

The synthesis route of CQM is shown in the Fig. 1a. Transmission electron microscopy (TEM) and scanning electron microscope (SEM) reveal that the morphology of CQM is the sheet-like structure, as shown in Fig. 1b and Fig. S1. The corresponding element mapping images of CQM provided in Fig. 1c–h exhibit the morphology and uniform distribution of C, O, N, S and Na elements. Moreover, Fourier transform infrared spectroscopy (FTIR) spectrum (Fig. 1i) illustrates that there are functional groups on CQM, including O–H, C–O, C=C and C=O bonds [13,34]. The characteristic peaks at 3400 and 1647 cm^{-1} correspond to the stretching vibrations of O–H and C=O, respectively, while the main characteristic peaks between 1602 and 1297 cm^{-1} and 1162 – 994 cm^{-1} are related to the stretching vibrations of C=C and C–O [35], respectively. In addition, the X-ray diffraction (XRD) pattern proves that CQM has a crystal structure (Fig. S2). Above results declare that CQM has a crystal structure and rich in functional groups. Next, ultraviolet-visible (UV-Vis) absorption spectrum indicates that CQM has a wide spectral response range in the UV to visible range (Fig. 1j).

Furthermore, Fig. 1k and Fig. S3 show the deconvoluted C 1s, O 1s and N 1s X-ray photoelectron spectroscopy (XPS) spectra of CQM, respectively, and Table S1 displays the elemental compositions of CQM.

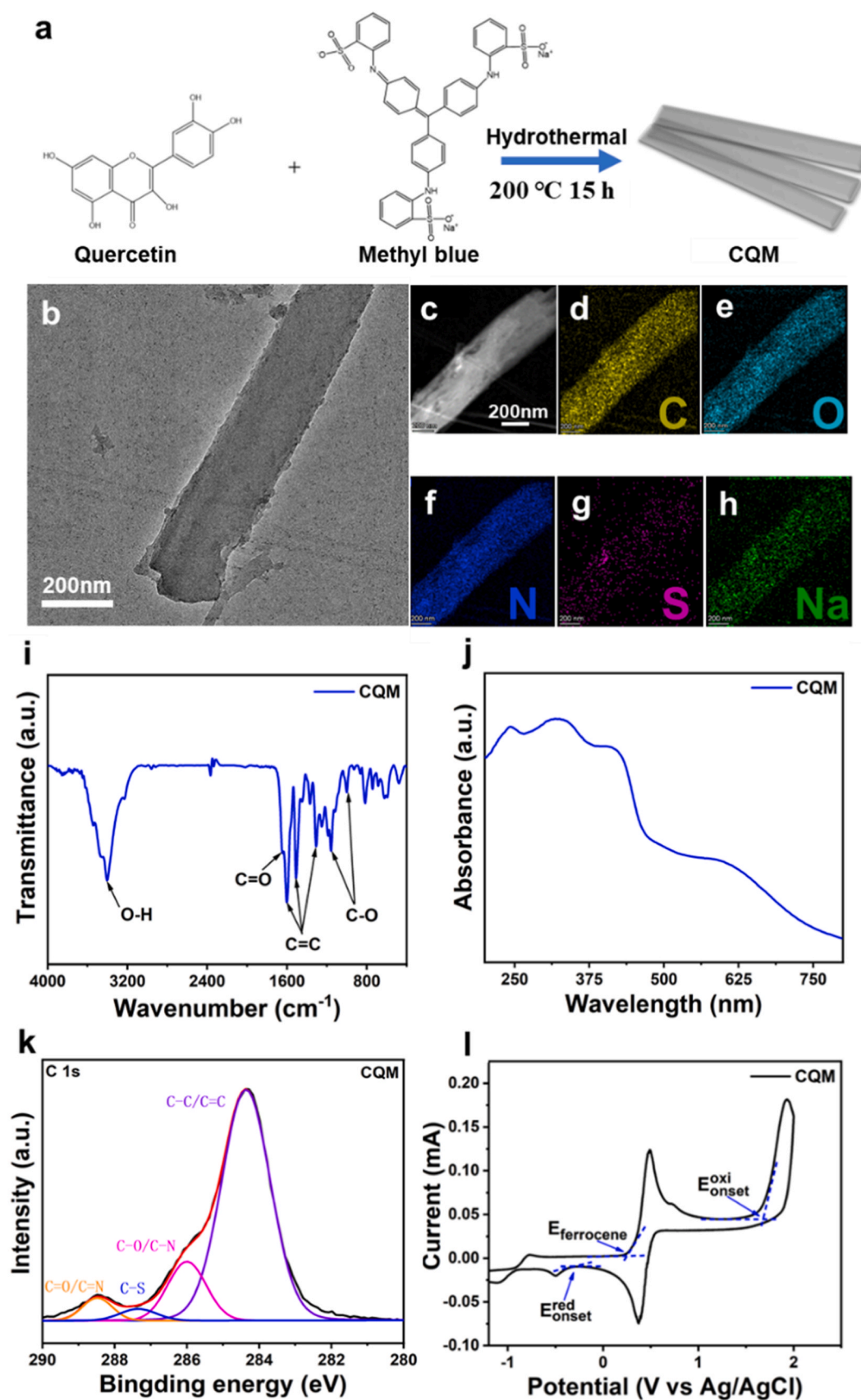


Fig. 1. (a) The schematic diagram for the synthesis of the CQM. (b) TEM image, (c) HAADF-STEM image and the elemental mapping images for (d) C, (e) O, (f) N, (g) S, and (h) Na elements of CQM. (i) FTIR spectrum, (j) UV-Vis absorption spectrum, (k) C 1s XPS spectra and (l) CV curve of CQM.

The C 1s spectra of CQM provided in Fig. 1k show four peaks at 291.5, 288.4, 285.9 and 284.3 eV, corresponding to C=O/C=N, C-S, C-O/C-N and C=C/C-C bonds, respectively [14,36,37]. The O 1s spectra of CQM in Fig. S3a reveal two peaks at 532.6 and 531.5 eV, representing C-O and C=O bonds respectively [38,39].

After the different ions (Mg^{2+} , Ca^{2+} , Al^{3+} and K^{+}) were added respectively to the reaction bottle, the structure of CQM under illumination was explored again. First, FTIR spectrum reveal that catalysts still have same functional groups as primary CQM, as shown in Fig. S4. Then, C 1s spectra of CQM with the addition of Mg^{2+} , Ca^{2+} , Al^{3+} and K^{+} respectively are shown in Fig. S5a. The characteristic peaks at 282.5, 287.5, 285.9 and 284.3 eV correspond to C=O/C=N, C-S, C-O/C-N and C=C/C-C bonds, respectively [39,40]. In addition, the O 1s spectra of CQM with the addition of four metal ions are shown in Fig. S5b. The two peaks at 532.7 and 531.5 eV are ascribed to C-O and C=O bonds, which is consistent with the primary CQM [38]. It can be deduced that the addition of metal ions did not change the composition and structure of CQM.

The band structure of CQM was explored by cyclic voltammetry (CV) experiment, with the ferrocene redox system as the external standard. Two pairs of redox peaks in Fig. 1l were derived from ferrocene and the CQM catalyst itself. The highest occupied molecular orbital (HOMO) and lower unoccupied molecular orbital (LUMO) energy levels of CQM are calculated as -6.21 eV and -4.40 eV, respectively [41]. The band gap obtained from CV is consistent with UV-Vis absorption spectrum [42]. The valance band (VB) of CQM is more positive than the electrochemical potential of $\text{O}_2/\text{H}_2\text{O}$ and the conduction band of CQM is more negative than the electrochemical potential of $\text{O}_2/\text{H}_2\text{O}$, as shown in Fig. S6. So CQM is able to produce H_2O_2 by oxygen reduction and water oxidation during the illumination [43].

3.2. Photocatalytic activities of CQM

The impact of various ions on the photocatalytic reaction of CQM were further investigated. As depicted in Fig. 2a–c, when there are no ions in the system, the photocatalytic H_2O_2 yield of CQM is $753 \mu\text{mol g}^{-1} \text{h}^{-1}$. And there is a positive correlation between the concentration of metal ions in the catalytic reaction and the yields of H_2O_2 . When the concentration of Mg^{2+} and Ca^{2+} ions reached 0.2 mol L^{-1} , the H_2O_2 yield on CQM was 4–5 times higher than that without metal ion, after which the H_2O_2 production rate increased at a slow pace. Specifically, when the concentration of Mg^{2+} was 0.36 mol L^{-1} , the yield of H_2O_2 reached its peak value at $12,812 \mu\text{mol g}^{-1} \text{h}^{-1}$. In contrast, for Al^{3+} , the yield of H_2O_2 ceased to increase when the ion concentration reached 0.06 mol L^{-1} .

It is interesting to note that the addition of K^{+} showed a different trend (Fig. 2d) to produce H_2O_2 . Unlike Mg^{2+} , Ca^{2+} , and Al^{3+} , adding K^{+} to the catalytic system resulted in a decrease in H_2O_2 yield. This finding aligns with the result obtained from TPV tests examining the influence of ions on CQM's photocatalytic performance, which will be discussed later.

The effects of adding Mg^{2+} , Ca^{2+} , Al^{3+} and K^{+} on the band structure of CQM were explored by CV test, respectively, as shown in Fig. 3a–c and Fig. S7. The LUMO and HOMO energy levels for CQM with various metal ions were as follows: Mg^{2+} (-4.13 eV, -6.29 eV), Ca^{2+} (-4.24 eV, -6.22 eV), Al^{3+} (-4.13 eV, -6.29 eV), and K^{+} (-4.17 eV, -6.20 eV). As shown in Fig. 3d, after adding metal ions in the catalytic system, the band gap of CQM increased slightly compared with the original catalyst. However, the VB and CB of CQM catalyst still meet the thermodynamic requirements of H_2O_2 production, indicating that the addition of metal ions does not change the dual-channel pathway for production of H_2O_2 .

TPV was applied to investigate the effect of ions on the catalytic

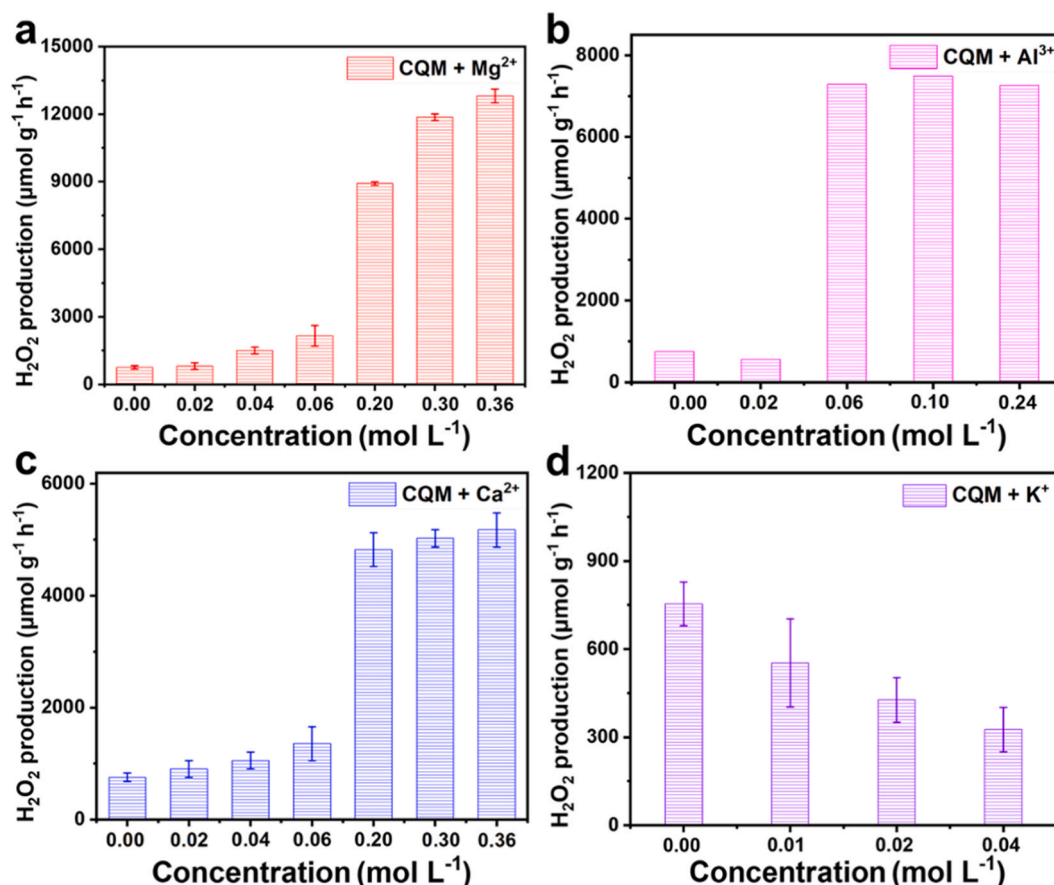


Fig. 2. H_2O_2 production rate varies with metal ion concentration in different salt solutions: (a) Mg^{2+} , (b) Ca^{2+} , (c) Al^{3+} and (d) K^{+} .

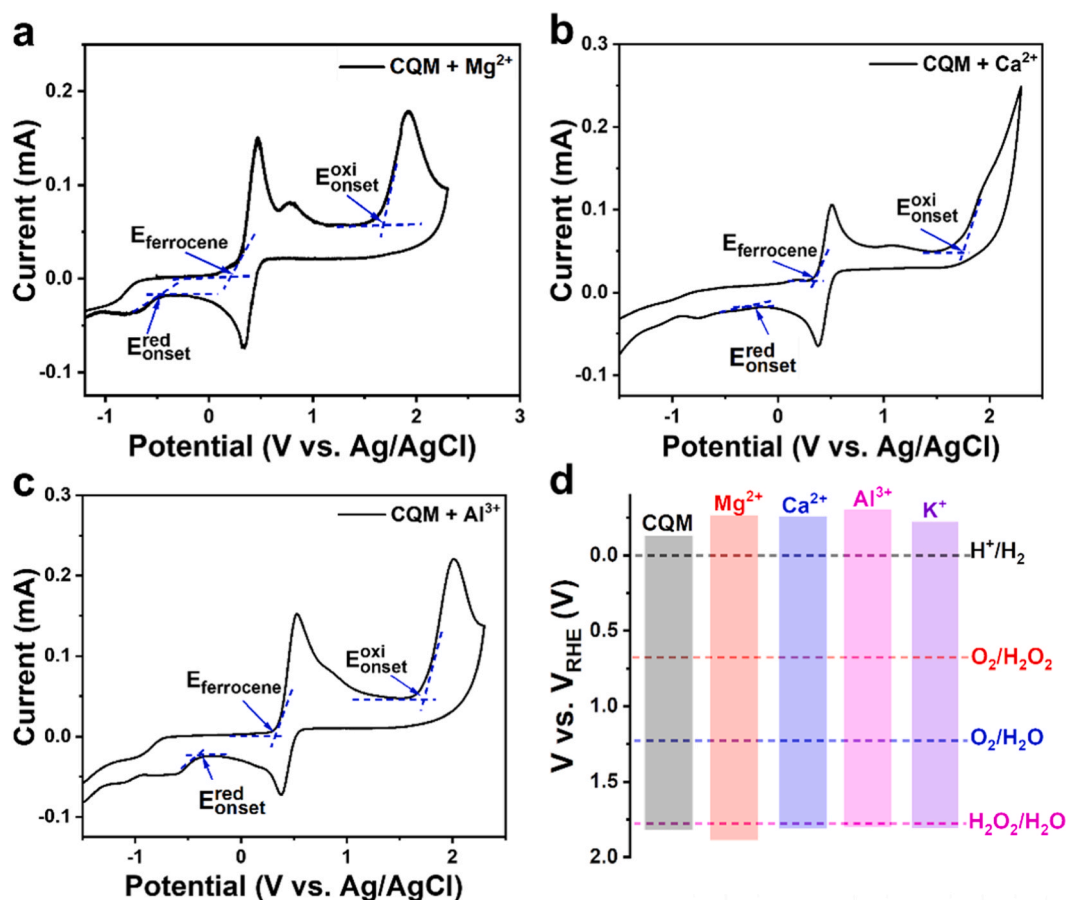


Fig. 3. The CV curves of CQM with the addition of different metal ions: (a) Mg^{2+} , (b) Ca^{2+} and (c) Al^{3+} . (d) Band structure diagram of CQM with the addition of different metal ions.

activity of CQM catalyst. The catalyst (30 mg) was mixed with MgCl_2 (0.001 mol), AlCl_3 (0.001 mol), CaCl_2 (0.001 mol) and KCl (0.001 mol) respectively and lyophilized. Then the lyophilized sample was excited under the same conditions as the original catalyst CQM.

Take the TPV curves of the Mg^{2+} added sample as an example. As shown in Fig. 4a, when the sample is excited, a signal is generated, which decays rapidly and produces a negative signal due to the influence of the electron sink effect [43]. The negative signal decays over time until it reaches zero, while the integral of the reverse signal over time is the amount of “trapped” charge (Q). After Mg^{2+} was added, Q of CQM was calculated to be 4.05 (Fig. 4b). As shown in Fig. 4c, before the negative signal, the material rapidly generates a positive signal and decays under laser excitation. The time required for the signal to reach its maximum value is defined as charge extraction rate (t_{max}), and the integral of the signal over this period is defined as maximum electron extraction (A). With the addition of Mg^{2+} on CQM, $t_{\text{max}} = 0.02631$ ms and $A = 0.02566$. The signals of other samples were also analyzed in the same way (Figs. S8 and S9). The Q, A and t_{max} of all samples are shown in Fig. 4b and d, respectively.

The charge in the negative region of the CQM with the addition of Mg^{2+} , Ca^{2+} , Al^{3+} , and K^+ are 4.05, 3.80, 2.90, and 1.20, respectively. As shown in Fig. 4b, Q changed a lot with the addition of different ions. CQM interacting with different ions (except K^+) produced more charges (Q) than the original catalyst, which means the negative region generated by charges recombination during attenuation was expanded, leading to an increased energy barrier of the electron sink. With the higher energy barrier of the electrons, more and more electrons are stored, and then sufficient electrons participated in the photocatalytic reaction to produce H_2O_2 . In addition, to better explore the effect of different ions on the photocatalyst, three important parameters, the

electron attenuation constants (τ), t_{max} and A of CQM were further calculated with the addition of metal ions, where τ represents the rate of electron decay. τ and A for different ions were compared in Fig. 4d (τ was analyzed in Fig. S9b). Although A and τ of CQM are the largest, it has the shortest t_{max} . Therefore, the n_e ($n_e = A \cdot \tau / t_{\text{max}}$) of CQM is low. In Fig. 4e, it can be observed that n_e of CQM with the addition of K^+ is lower than that of CQM without the addition of metal ions. The low value of n_e and small τ of CQM with the addition of K^+ lead to the decrease of the catalytic activity. Using the n_e , it can be deduced that the order of catalyst activity with the addition of different ions is $\text{Mg}^{2+} > \text{Al}^{3+} > \text{Ca}^{2+} > \text{K}^+$.

TPV measurements were further performed to explore the photocatalytic properties and charge transfer process on CQM. In Fig. 5a, the principle of TPV measurement is schematically illustrated. Firstly, CQM was coated on an ITO electrode, and then different MeCN solutions (N_2 saturated, O_2 saturated, and 0.5 vol% H_2O) were sprayed onto the CQM film to form a thin liquid layer. Next, the CQM was excited by a pulsed laser of 355 nm (5 ns) and the TPV signal was simultaneously collected by a computer. Under N_2 saturated MeCN, the photoelectrons of CQM were transferred to the ITO electrode. In contrast, under O_2 saturated MeCN or 0.5 vol% $\text{H}_2\text{O}/\text{MeCN}$ (V / V), O_2 or H_2O will consume electrons or holes, resulting in the change of signals. The more electrons collected by ITO electrode, the stronger the photovoltage intensity.

As depicted in Fig. 5b, the CQM in the MeCN solution containing 5 % water displayed the higher photovoltage than the CQM in the N_2 saturated MeCN where H_2O consumed the holes of $\Delta Q_1 = 0.0272$ in the water oxidation reaction. According to Fig. 5c, CQM in the O_2 saturated MeCN consumed a lot of electrons, and the amount of charge consumed by oxygen reduction is $\Delta Q_2 = 0.1527$. For $\Delta Q_2 = 0.1527 > \Delta Q_1 = 0.0272$, it can be inferred that the rate of oxygen reduction is greater

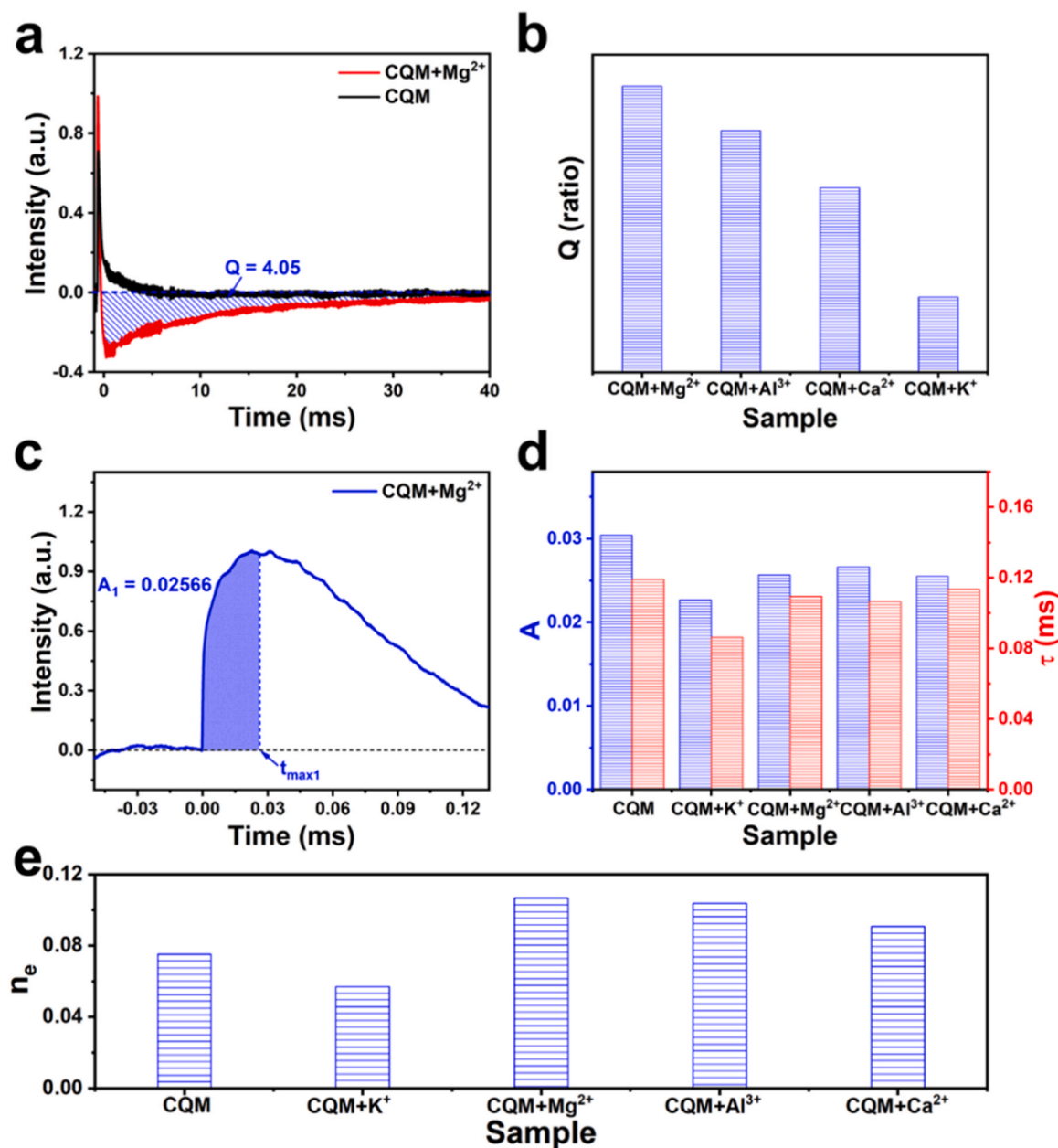


Fig. 4. (a) TPV curves of CQM and CQM with the addition of Mg²⁺. (b) Q of CQM with the addition of different metal ions. (c) The t_{max} and A of CQM with the addition of Mg²⁺. (d) A and τ of CQM with and without the addition of different metal ions. (e) n_e of CQM and CQM with the addition of different metal ions.

than that of water oxidation. τ is the evaluation of the charge recombination rate. The order of $\tau_1 = 0.218 \text{ ms} > \tau_2 = 0.209 \text{ ms} > \tau_3 = 0.201 \text{ ms}$ (Fig. S10).

3.3. Using ML to explore the interactions between metal ions and H₂O₂ yield

ML with its ability to effectively predict performance and analyze relationships within multi-dimensional data [44–48], was utilized to further investigate the interactions of metal ions in the multi-ions system and to identify the multi-ions environment that allows CQM to exhibit optimal photocatalytic performance.

A dataset was constructed by setting multi-ions concentrations as features (including Mg²⁺, Ca²⁺, Al³⁺, K⁺, and Na⁺), as shown in Table S3. Each metal ion are set with three different concentrations: 0 mol L⁻¹, 0.12 mol L⁻¹, and 0.24 mol L⁻¹. Experiments were then conducted according to the dataset, with their H₂O₂ yields recorded. The

recorded H₂O₂ yields, combined with the dataset, served as input for the ML model.

The Pearson's correlation coefficient heat map (Fig. 6a) shows that features were independent of each other. Then, the dataset was randomly shuffled and split into training and testing datasets at an 8:2 ratio. The training and testing datasets were used to train the model and evaluate its performance, respectively. The performance of different models was assessed using the coefficient of determination (R²) and mean square error (MSE). Among Gradient Boosting Regression (GBR), Decision Tree Regressor (DTR), XGB Regressor (XGBR), and K Neighbors Regressor (KNN_reg) models, XGBR outperformed others with the highest R² and lowest MSE (Fig. 6b). The regression curve of training data versus test data demonstrates that XGBR has good generalization data (Fig. 6c). Feature importance was calculated based on XGBR (Fig. 6d), which aligns with the n_e order (Mg²⁺ > Al³⁺ > Ca²⁺ > K⁺) from the TPV test.

Using prediction capabilities of ML, several optimal combinations of

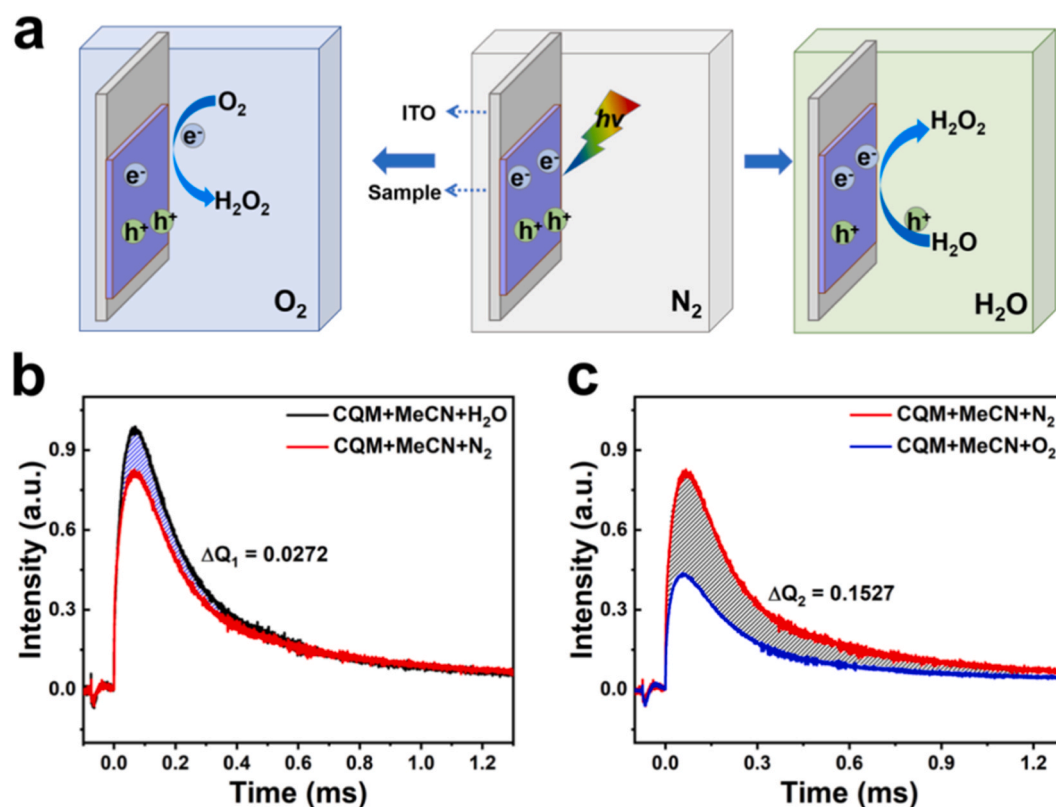


Fig. 5. (a) The schematic of in-situ TPV test under different atmospheres. (b) TPV curves of CQM under H_2O -saturated MeCN and N_2 -saturated MeCN. (c) TPV curves of CQM under N_2 -saturated MeCN and O_2 -saturated MeCN.

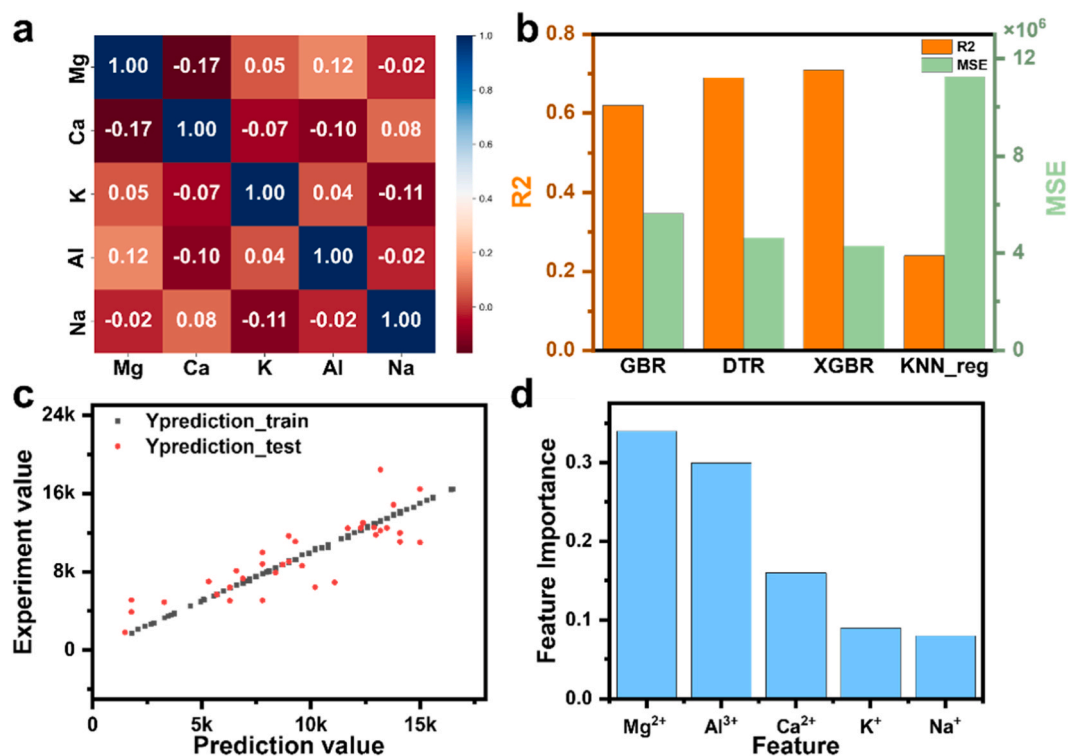


Fig. 6. (a) The Pearson's correlation coefficient heat map of features. (b) ML models assessed by R2 and MSE. (c) Regression curve of prediction data (black dots) and experiment data (red dots) for the XGBR model. (d) Features importance of the five metal ions.

metal ion concentrations were identified by XGBR. Table S4 lists the prediction of XGBR model that these combinations can maximize CQM's photocatalytic yield to $19465 \mu\text{mol g}^{-1} \text{h}^{-1}$ (Table S4). While the experiment result shows that the maximum can reach $19,560 \mu\text{mol g}^{-1} \text{h}^{-1}$. In the same time, the experiment result and the prediction result match well, which proves the validity of the model predictions.

Due to the high complexity of the metal ion composition-performance relationship and the apparent noise from experimental measurements, it remains challenging to produce a clear mathematical equation to describe the interactions between metal ions. However, recent advances in the field of interpretable ML provide new avenues for quantifying the interactions between input features and their correlation with prediction values. To explore metal ions interfere contributions to the photocatalytic process in complex ionic systems, we used SHAP values to further analyze the data. SHAP is a model interpretation

package developed in Python that can explain the output of any machine learning model. Its name comes from the SHapley Additive exPlanation, and under the inspiration of cooperative game theory, SHAP constructs an additive explanation model where all features are considered as "contributors" [49]. For each predicted sample, the model produces a predicted value, and the SHAP value is assigned to each feature in that sample. A positive SHAP value means that the features promote H_2O_2 yield, while a negative SHAP value means that the features inhibit H_2O_2 yield.

Fig. 7a shows the distribution of SHAP values for the metal ions interactions on CQM's H_2O_2 yield in multi-ion systems. The interactions of metal ions on the system is highly complex as the types and concentrations of metal ions change. To explore those interactions, we used the form of Fig. 7b–e to plot the interactions between metal ions and marked the concentrations of the two ions. As shown in Fig. 7b, when Mg^{2+} and

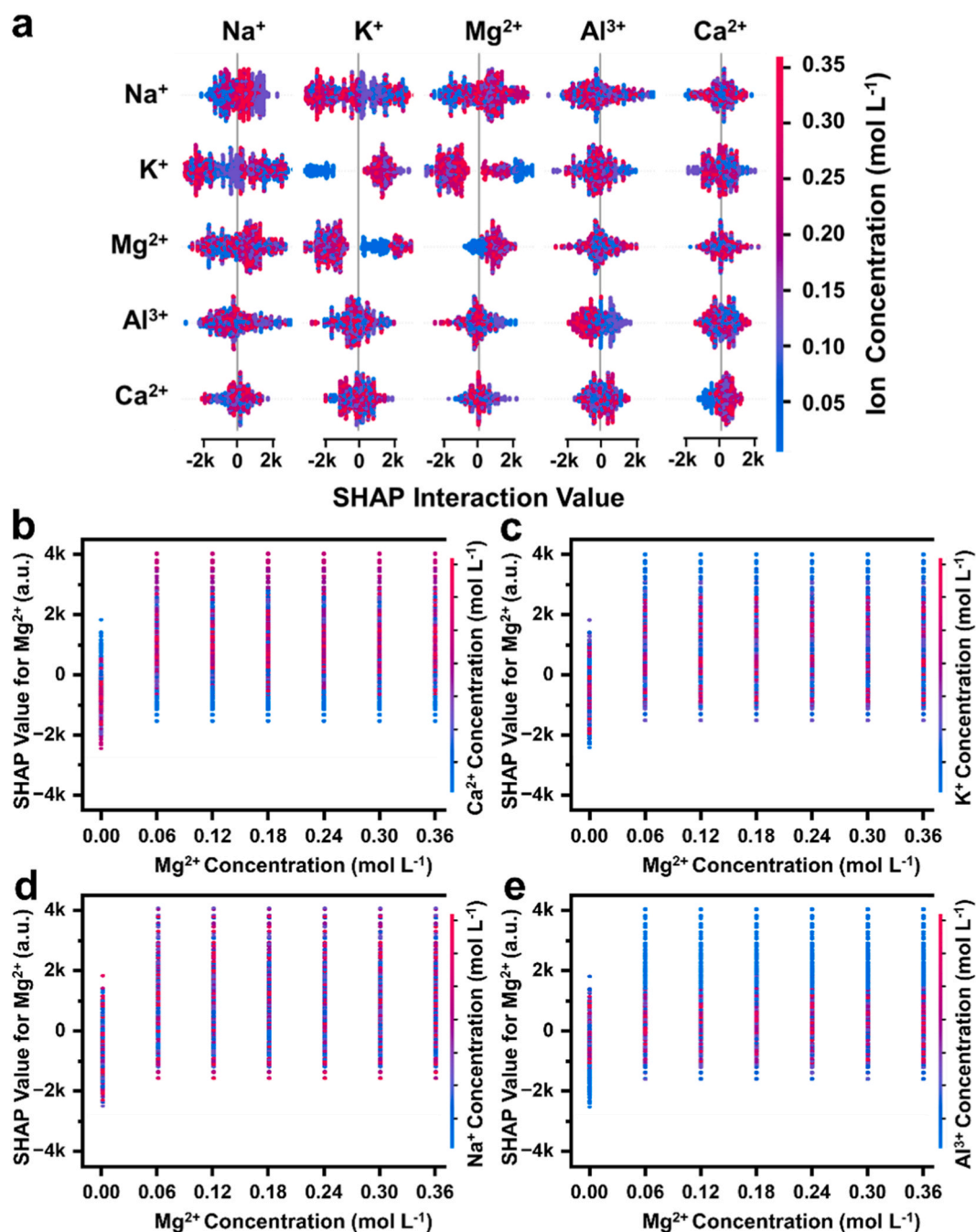


Fig. 7. (a) Interaction diagram of five metal ions and interaction diagram of Mg^{2+} with (b) Ca^{2+} , (c) K^+ , (d) Na^+ , and (e) Al^{3+} .

Ca^{2+} are presented together. Their interaction always causes the system's SHAP values to increase, meaning that their interaction can promote H_2O_2 yield. As shown in Fig. 7c, for Mg^{2+} and K^+ , their interaction causes a increase in the system's SHAP value, but if Mg^{2+} is to make its maximum contribution, K^+ concentration should be 0 mol L^{-1} . As shown in Fig. 7d, when Mg^{2+} and Na^+ are presented together, the system's SHAP value increases compared to when Na^+ is not present, meaning that Na^+ increases Mg^{2+} 's contribution to H_2O_2 . As shown in Fig. 7e, for Mg^{2+} and Al^{3+} , when neither is presented, the model gives a SHAP value of -1000 to 2000 for the system, meaning that their individual presence will promote an increase in H_2O_2 yield. However, when both are presented, they interfere with each other's contributions to H_2O_2 yield. As can be seen, when Al^{3+} is not presented, Mg^{2+} can make the greatest contribution to H_2O_2 yield, with a system SHAP value of up to 4000. However, when both are presented, the system's SHAP value can only be within the range of -1000 – 1000 .

As shown in Fig. 8, for K^+ , when its concentration is below 0.18 mol L^{-1} , its interaction with other metal ions causes a slight increase in SHAP values; when its concentration reaches 0.18 mol L^{-1} or higher, its interaction with other metal ions rapidly reduces the system's SHAP values. As shown in Fig. S11, when the concentration of Ca^{2+} is 0.12 mol L^{-1} or below, its interaction with other ions causes the SHAP value of the system to rise. However, when the concentration of Ca^{2+} reaches 0.18 mol L^{-1} or above, its interaction with K^+ and Mg^{2+} becomes obviously weaker, and the SHAP value of the system shows a downward trend. As shown in Fig. S12, for Na^+ , its presence allows other metal ions to increase their own contributions to H_2O_2 yield. And from Fig. S13, it can be seen that when Al^{3+} concentration is at or below 0.18 mol L^{-1} , its interaction with Ca^{2+} increases the system's SHAP value; when Al^{3+} concentration increases further, the system's SHAP value decreases.

Fig. 9 illustrates the schematic of the five metal ion interactions. The color of the lines in the figure represents whether the interaction between ions promotes (red) or inhibits H_2O_2 (blue). Half-red half-blue lines indicate that the effects of interaction change with concentrations. The thickness of the lines represents the magnitude of the interaction. It

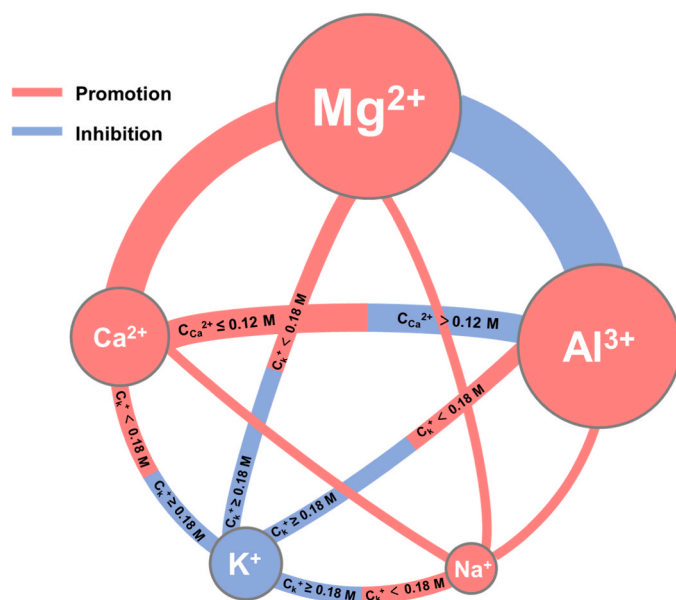


Fig. 9. Schematic diagram of the five metal ionic interactions.

can be observed that Na^+ promotes H_2O_2 yield with its interactions with all ions except K^+ , and these interactions are relatively smaller compared to others. The interactions of K^+ with other ions are larger than those of Na^+ with other ions. When K^+ 's concentration is below 0.18 mol L^{-1} , its interactions with other metal ions promote H_2O_2 yields, while at higher concentrations, they inhibit it. The interactions of Ca^{2+} with Al^{3+} and K^+ with Al^{3+} are similar, while the interaction of Ca^{2+} with Mg^{2+} consistently promotes H_2O_2 yield. The interaction between Mg^{2+} and Al^{3+} always inhibits H_2O_2 yields. Overall, ion interactions primarily promote H_2O_2 yields. Therefore, it can be inferred that multiple ions in seawater can enhance the H_2O_2 yields of CQM in seawater.

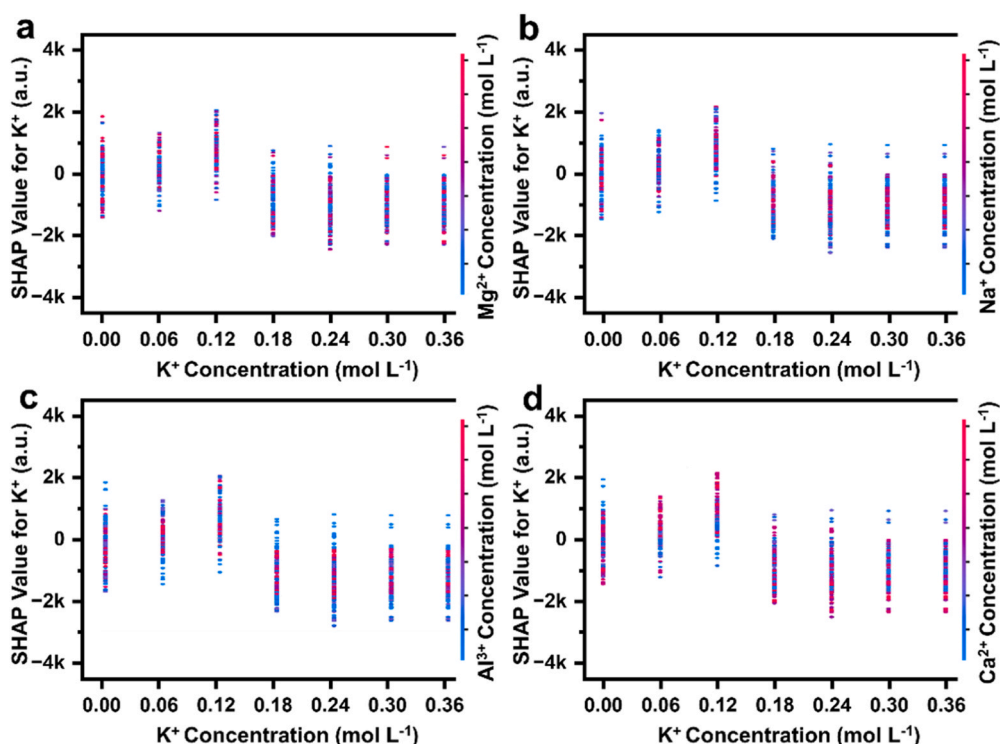


Fig. 8. Interaction diagram of K^+ with (a) Mg^{2+} , (b) Na^+ , (c) Al^{3+} , and (d) Ca^{2+} .

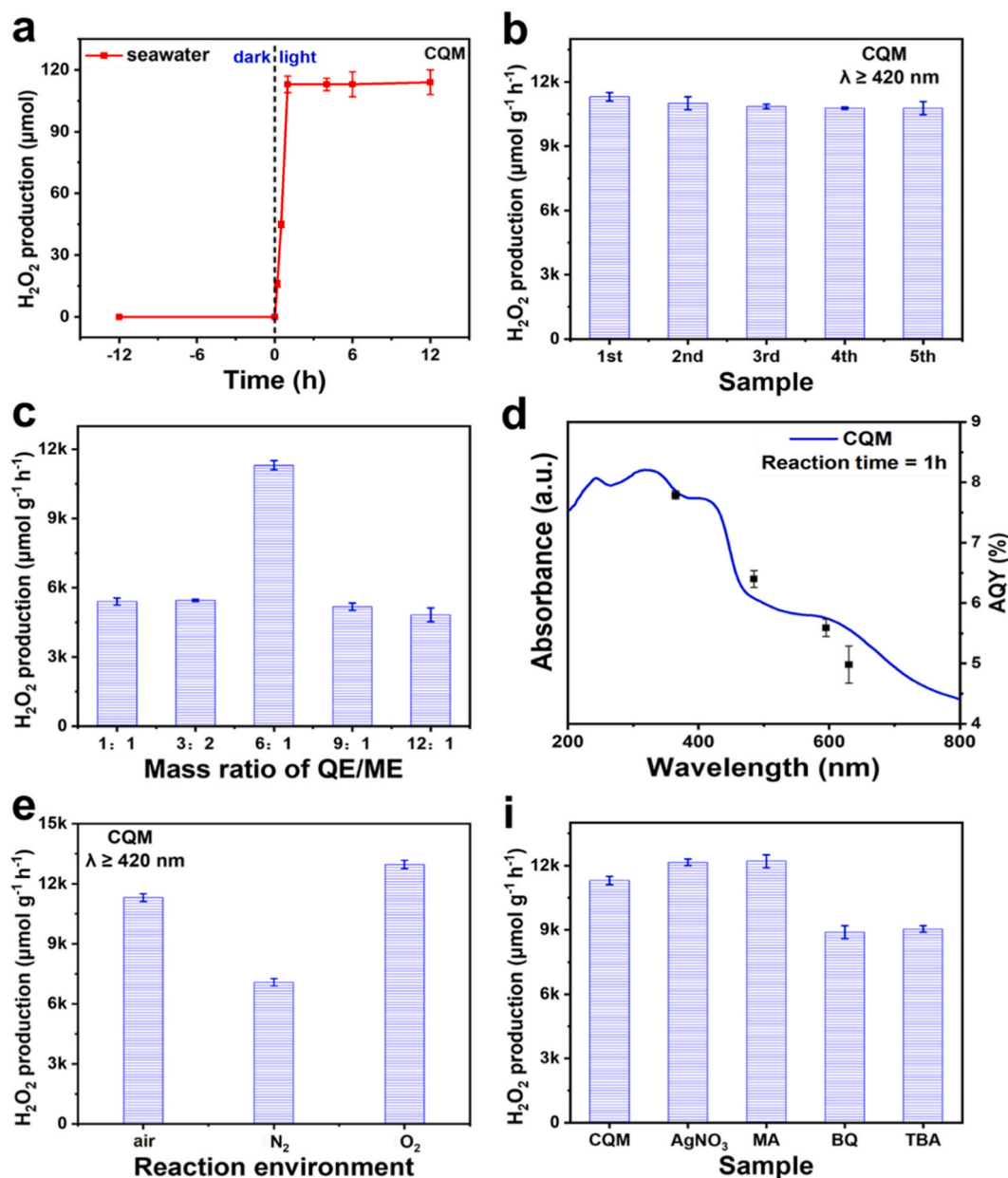


Fig. 10. (a) The H₂O₂ yields curve over time of CQM (10 mg) in seawater. (b) The cycling stability of CQM in seawater. (c) The yields of H₂O₂ of catalysts obtained by CQM synthesis method with different mass ratios of quercetin and methyl blue. (d) The UV-vis absorption spectrum and corresponding quantum efficiency (AQY) at different wavelengths of incident light (365, 485, 595, and 630 nm). (e) The H₂O₂ yields of CQM in different gas environments. (f) The H₂O₂ yields of CQM after adding different sacrificial agents.

3.4. Photocatalytic performance of CQM in seawater

We further examined the photocatalytic performance of CQM in seawater. Fig. 10a illustrates the trend of H₂O₂ production over time. It is observed that no H₂O₂ was detected in seawater under dark reacting for 12 h, indicating no dark reaction. The production of H₂O₂ by CQM as a photocatalyst increased with illumination time in the early stages of the catalytic reaction, but plateau after 1 h.

The photocatalytic stability of CQM in seawater was also investigated. Fig. 10b shows that there was no significant decrease in the H₂O₂ production rate (11306 μmol g⁻¹ h⁻¹) during 5 cycling tests within a 1 h photocatalytic period. The TEM image (Fig. S14) shows that the structure of CQM retains intact after the photocatalytic reaction. The full XPS spectra after the catalytic reaction (Fig. S15a) display numerous signal peaks of elements, primarily due to adsorbed ions and impurities from

seawater. However, no significant changes appear in the C 1 s and O 1 s spectra of CQM (Fig. S15b–c). We also explored how the ratio of quercetin to methyl blue components in raw materials, the hydrothermal temperature and hydrothermal time affected the photocatalytic performance of CQM. The optimal H₂O₂ yield of 11306 μmol g⁻¹ h⁻¹ was achieved when the quercetin to methyl blue ratio, hydrothermal temperature and time were 6:1, 200 °C and 15 h, respectively, as shown in Fig. 10c and Fig. S16. Fig. 10d shows that the apparent quantum yield (AQY) curve's variation tendency aligns with its optical absorption spectrum, suggesting that H₂O₂ production is driven by the absorbed photon. The AQY of CQM coincided with the UV-Vis spectrum, reaching 7.79 % (Table S2) under excitation light at 365 nm.

The photocatalytic performance of CQM in seawater under different atmospheres (air, N₂, O₂) was also explored (Fig. 10e), and the photocatalytic pathway for H₂O₂ production was inferred. The H₂O₂ yield did

not significantly reduce in the deionized water bubbled with N_2 for 60 min, suggesting a pathway for H_2O_2 production through water oxidation when O_2 is absent or minimal. Moreover, the generation rate of H_2O_2 in O_2 saturated seawater water was faster than that in N_2 saturated seawater water, indicating the participation of O_2 in the catalytic reaction. These results demonstrate that H_2O_2 production can occur through both oxygen reduction and water oxidation in the photocatalytic system.

To gain a deeper understanding of the photocatalytic reaction mechanism, active species trapping experiments were conducted. These experiments aim to determine the role of different active species in the reaction. $AgNO_3$, methanol, benzoquinone, and tertiary butanol were added as trapping agents for electrons (e^-), holes (h^+), superoxide, and hydroxyl radicals, respectively [50]. The production of H_2O_2 increased with the addition of $AgNO_3$ and methanol (Fig. 10f), suggesting that both electrons and holes contribute to H_2O_2 generation. On the other hand, the addition of benzoquinone and tertiary butanol led to a decrease in H_2O_2 production, indicating that both superoxide and hydroxyl radicals also play a role in H_2O_2 generation.

Electron paramagnetic resonance (EPR) experiments were then performed to provide direct evidence for the involvement of these reactive species. Fig. S17 shows signals for $\cdot O_2^-$ (with a typical intensity ratio of 1:1:1:1) and $\cdot OH$ (with a typical intensity ratio of 1:2:2:1) after illumination, confirming their generations in the photocatalytic reaction. The absence of $\cdot OH$ radical and $\cdot O_2^-$ signals under dark conditions confirmed that these species were not generated in the dark reaction, indicating that the catalyst did not react under dark condition.

The reaction mechanism was further investigated using electrochemical testing. Transient photocurrent response (TPR) measurements were conducted to assess the catalyst's photo-response characteristics in seawater. The photocurrent curves for CQM collected under open circuit potential and lighting with 30 s light on/off cycles ($\lambda \geq 420$ nm) showed strong photocurrent induction by CQM (Fig. S18a), indicating efficient charge separation. Electrochemical impedance spectroscopy (EIS) was performed in the frequency range of 1 MHz - 0.01 Hz to examine the catalyst's charge transferability in seawater (Fig. S18b). The small circular radius of CQM suggests a faster rate of interfacial electron transfer for CQM. In conclusion, these findings suggest that H_2O_2 is produced by both water oxidation and oxygen reduction which are consistent with the result of TPV.

4. Conclusions

In summary, we developed a new carbon-based catalyst, CQM, and investigated the effects of metal ion interactions on H_2O_2 yield in a photocatalytic system. We discovered that this kind of metal ions effects on photocatalytic activity with effect order of $Mg^{2+} > Al^{3+} > Ca^{2+} > K^+$. In present system, when the Mg^{2+} concentration reached 0.36 mol L^{-1} , the H_2O_2 yield was as high as 12,812 $\mu mol g^{-1} h^{-1}$. We also employed machine learning to further discover the interaction of metal ions on the H_2O_2 photoproduction. By tuning the concentration of multiple metal ions, with CQM as catalyst, the H_2O_2 yield can reach 19,560 $\mu mol g^{-1} h^{-1}$. Finally, we tested the photocatalytic ability of CQM in seawater and found that its yield can reach 11306 $\mu mol g^{-1} h^{-1}$. Our catalytic system not only provides a novel approach for photocatalytic H_2O_2 production in seawater but also offers a promising strategy for designing, selecting, and optimizing photocatalysts.

Supporting information

Experimental section and additional figures.

CRediT authorship contribution statement

Jiacheng Li: Conceptualization, Formal analysis, Writing – Original Draft. **Hong Shi:** Formal analysis, Writing – Original Draft. **Zenan Li:**

Investigation. **Jiaxuan Wang:** Investigation. **Honglin Si:** Investigation. **Fan Liao:** Writing – review & editing, Supervision. **Hui Huang:** Writing – review & editing, Supervision. **Yang Liu:** Supervision, Funding acquisition. **Zhenhui Kang:** Supervision, Funding acquisition, Writing – review & editing.

Declaration of Competing Interest

The authors declare that they have no known competing financial interests or personal relationships that could have appeared to influence the work reported in this paper.

Data Availability

Data will be made available on request.

Acknowledgements

This work is supported by Natural Science Foundation of Jiangsu Province (BK20220028), National MCF Energy R&D Program of China (2018YFE0306105), National Key R&D Program of China (2020YFA0406104, 2020YFA0406101), Innovative Research Group Project of the National Natural Science Foundation of China (51821002), National Natural Science Foundation of China (51972216, 52272043, 52271223, 52202107, 52201269), Natural Science Foundation of Jiangsu Province (BK20210735, 21KJB430043), The Science and Technology Development Fund, Macau SAR (0009/2022/ITP), Collaborative Innovation Center of Suzhou Nano Science & Technology, the 111 Project, and Suzhou Key Laboratory of Functional Nano & Soft Materials.

Appendix A. Supporting information

Supplementary data associated with this article can be found in the online version at doi:10.1016/j.apcatb.2023.123541.

References

- [1] L. Zhou, J.Y. Lei, F.C. Wang, L.Z. Wang, M.R. Hoffmann, Y.D. Liu, S.I. In, J. L. Zhang, Carbon nitride nanotubes with in situ grafted hydroxyl groups for highly efficient spontaneous H_2O_2 production, *Appl. Catal. B: Environ.* 288 (2021), 119993.
- [2] L. Zhou, J.R. Feng, B.C. Qiu, Y. Zhou, J.Y. Lei, M.Y. Xing, L.Z. Wang, Y.B. Zhou, Y. D. Liu, J.L. Zhang, Ultrathin g- C_3N_4 nanosheet with hierarchical pores and desirable energy band for highly efficient H_2O_2 production, *Appl. Catal. B: Environ.* 267 (2020), 118396.
- [3] J.J. Cao, Q.Y. Wu, Y.J. Zhao, K.Q. Wei, Y. Li, X. Wang, F. Liao, H. Huang, M. W. Shao, Y. Liu, Z.H. Kang, In-situ photovoltage transients assisted catalytic study on H_2O_2 photoproduction over organic molecules modified carbon nitride photocatalyst, *Appl. Catal. B: Environ.* 285 (2021), 119817.
- [4] Z.C. Jiang, B. Cheng, Y. Zhang, S. Wageh, A.A. Al-Ghamdi, J.G. Yu, L.X. Wang, S-scheme ZnO/WO₃ heterojunction photocatalyst for efficient H_2O_2 production, *J. Mater. Sci. Technol.* 124 (2022) 193–201.
- [5] H. Zhang, M. Liu, X.Y. Zhang, B.A. Yuan, P. Wu, C.J. Liu, W. Jiang, On-site H_2O_2 production with amphiphilic g- C_3N_4 as photocatalyst in a combined photocatalysis-extraction-separation process, *Chem. Eng. J.* 438 (2022), 135664.
- [6] L.H. Zheng, H.R. Su, J.Z. Zhang, L.S. Walekar, H.V. Molamahmood, B.X. Zhou, M. C. Long, Y.H. Hu, Highly selective photocatalytic production of H_2O_2 on sulfur and nitrogen for co-doped graphene quantum dots tuned TiO₂, *Appl. Catal. B: Environ.* 239 (2018) 475–484.
- [7] Y.J. Zhao, Y. Liu, Z.Z. Wang, Y.R. Ma, Y.J. Zhou, X.F. Shi, Q.Y. Wu, X. Wang, M. W. Shao, H. Huang, Y. Liu, Z.H. Kang, Carbon nitride assisted 2D conductive metal-organic frameworks composite photocatalyst for efficient visible light-driven H_2O_2 production, *Appl. Catal. B: Environ.* 289 (2021), 120035.
- [8] Y.J. Zhao, Y. Liu, J.J. Cao, H. Wang, M.W. Shao, H. Huang, Y. Liu, Z.H. Kang, Efficient production of H_2O_2 via two-channel pathway over ZIF-8/ C_3N_4 composite photocatalyst without any sacrificial agent, *Appl. Catal. B: Environ.* 278 (2020), 119289.
- [9] J.Z. Zhang, J.Y. Lang, Y. Wei, Q. Zheng, L.Y. Liu, Y.H. Hu, B.X. Zhou, C.L. Yuan, M. C. Long, Efficient photocatalytic H_2O_2 production from oxygen and pure water over graphitic carbon nitride decorated by oxidative red phosphorus, *Appl. Catal. B: Environ.* 298 (2021), 120522.

- [10] Y. Yang, B.C. Zhu, L.B. Wang, B. Cheng, L.Y. Zhang, J.G. Yu, In-situ grown N, S co-doped graphene on TiO₂ fiber for artificial photosynthesis of H₂O₂ and mechanism study, *Appl. Catal. B: Environ.* 317 (2022), 121788.
- [11] Y. Yang, H.C. Yu, M.Q. Wu, T.T. Zhao, Y.A. Guan, D. Yang, Y.F. Zhu, Y.Q. Zhang, S. C. Ma, J. Wu, L. Liu, T.J. Yao, Dual H₂O₂ production paths over chemically etched MoS₂/FeS₂ heterojunction: maximizing self-sufficient heterogeneous Fenton reaction rate under the neutral condition, *Appl. Catal. B: Environ.* 325 (2023), 122307.
- [12] H.Z. Wang, C. Yang, F.S. Chen, G.F. Zheng, Q. Han, A crystalline partially fluorinated triazine covalent organic framework for efficient photosynthesis of hydrogen peroxide, *Angew. Chem. Int. Ed.* 61 (2022), e202202328.
- [13] H. Shi, Q.Y. Wu, Z.Y. Wu, Y. Liu, X.T. Wang, H. Huang, Y. Liu, Z.H. Kang, A metal-free catalyst for the efficient and stable one-step photocatalytic production of pure hydrogen peroxide, *Catal. Sci. Technol.* 12 (2022) 1837–1842.
- [14] J.N. Zhang, Y.F. Lei, S. Cao, W.P. Hu, L.Y. Piao, X.B. Chen, Photocatalytic hydrogen production from seawater under full solar spectrum without sacrificial reagents using TiO₂ nanoparticles, *Nano Res.* 15 (2022) 2013–2022.
- [15] J.M. Campos-Martin, G. Blanco-Brieva, J.L. Fierro, Hydrogen peroxide synthesis: an outlook beyond the anthraquinone process, *Angew. Chem. Int. Ed.* 45 (2006) 6962–6984.
- [16] H. Hou, X. Zeng, X. Zhang, Production of hydrogen peroxide by photocatalytic processes, *Angew. Chem. Int. Ed.* 59 (2020) 17356–17376.
- [17] S.J. Freakley, Q. He, J.H. Harrihy, L. Lu, D.A. Crole, D.J. Morgan, E.N. Ntainjua, J. K. Edwards, A.F. Carley, A.Y. Borisevich, C.J. Kiely, G.J. Hutchings, Palladium-tin catalysts for the direct synthesis of H₂O₂ with high selectivity, *Science* 351 (2016) 965–968.
- [18] S. Siahrostami, A. Verdager-Casadevall, M. Karamad, D. Deiana, P. Malacrida, B. Wickman, M. Escudero-Escribano, E.A. Paoli, R. Frydendal, T.W. Hansen, I. Chorkendorff, I.E. Stephens, J. Rossmeisl, Enabling direct H₂O₂ production through rational electrocatalyst design, *Nat. Mater.* 12 (2013) 1137–1143.
- [19] J.K. Edwards, B. Solsona, E.N. N. A.F. Carley, A.A. Herzog, C.J. Kiely, G. J. Hutchings, Switching off hydrogen peroxide hydrogenation in the direct synthesis process, *Science* 323 (2009) 1037–1041.
- [20] C. Xia, Y. Xia, P. Zhu, L. Fan, H.T. Wang, Direct electrosynthesis of pure aqueous H₂O₂ solutions up to 20% by weight using a solid electrolyte, *Science* 366 (2019) 226–231.
- [21] C. Xia, S. Back, S. Ringe, K. Jiang, F. Chen, X. Sun, S. Siahrostami, K. Chan, H. Wang, Confined local oxygen gas promotes electrochemical water oxidation to hydrogen peroxide, *Nat. Catal.* 3 (2020) 125–134.
- [22] Q.L. Zhao, Y. Wang, W.H. Lai, F. Xiao, Y.X. Lyu, C.Z. Liao, M.H. Shao, Approaching a high-rate and sustainable production of hydrogen peroxide: oxygen reduction on Co-N-C single-atom electrocatalysts in simulated seawater, *Energy Environ. Sci.* 14 (2021) 5444–5456.
- [23] X. Guan, F.A. Chowdhury, N. Pant, L. Guo, L. Vayssieres, Z. Mi, Efficient unassisted overall photocatalytic seawater splitting on GaN-based nanowire arrays, *J. Phys. Chem. C* 122 (2018) 13797–13802.
- [24] J.N. Zhang, W.P. Hu, S. Cao, L.Y. Piao, Recent progress for hydrogen production by photocatalytic natural or simulated seawater splitting, *Nano Res.* 13 (2020) 2313–2322.
- [25] X.K. Zeng, Y. Liu, Y. Kang, Q. Li, Y. Xia, Y.L. Zhu, H.L. Hou, M.H. Uddin, T. R. Gengenbach, D.H. Xia, C. Sun, D.T. McCarthy, A. Deletic, J. Yu, X.W. Zhang, Simultaneously tuning charge separation and oxygen reduction pathway on graphitic carbon nitride by polyethylenimine for boosted photocatalytic hydrogen peroxide production, *ACS Catal.* 10 (2020) 3697–3706.
- [26] H. Luo, T.S. Shan, J.W. Zhou, L.L. Huang, L.H. Chen, R. Sa, Y. Yamauchi, J.M. You, Y. Asakura, Z.H. Yuan, H. Xiao, Controlled synthesis of hollow carbon ring incorporated g-C₃N₄ tubes for boosting photocatalytic H₂O₂ production, *Appl. Catal. B: Environ.* 337 (2023), 122933.
- [27] H.Y. Shi, Y. Li, X.F. Wang, H.G. Yu, J.G. Yu, Selective modification of ultra-thin g-C₃N₄ nanosheets on the (110) facet of Au/BiVO₄ for boosting photocatalytic H₂O₂ production, *Appl. Catal. B: Environ.* 297 (2021), 120414.
- [28] X. Yang, Z. Hu, Q. Yin, C. Shu, X.F. Jiang, J. Zhang, X. Wang, J.X. Jiang, F. Huang, Y. Cao, Water-soluble conjugated molecule for solar-driven hydrogen evolution from salt water, *Adv. Funct. Mater.* 29 (2019) 1808156.
- [29] Y. Liu, Y.J. Zhao, Q.Y. Wu, X. Wang, H.D. Nie, Y.J. Zhou, H. Huang, M.W. Shao, Y. Liu, Z.H. Kang, Charge storage of carbon dot enhances photo-production of H₂ and H₂O₂ over Ni₂P/carbon dot catalyst under normal pressure, *Chem. Eng. J.* 409 (2021), 128184.
- [30] P.P. Luo, X.Z. Li, B.B. Qu, H.Y. Xue, Y.H. Yang, Solar-driven seawater production H₂O₂ catalyzed by hydroxyl functionalized crystalline K-doped g-C₃N₄ under ambient conditions, *Appl. Organomet. Chem.* 37 (2023) 7264.
- [31] A. Gopakumar, T. Zhang, S. Das, Micro-Batch flow reactor for the photoproduction of H₂O₂ from water/real seawater, *J. Flow. Chem.* 13 (2023) 185–192.
- [32] A. Gopakumar, P. Ren, J.H. Chen, B.V.M. Rodrigues, H.Y.V. Ching, A. Jaworski, S. Van Doorslaer, A. Rokicinska, P. Kustrowski, G. Barcaro, S. Monti, A. Slabon, S. Das, Lignin-supported heterogeneous photocatalyst for the direct generation of H₂O₂ from seawater, *J. Am. Chem. Soc.* 144 (2022) 2603–2613.
- [33] J.Y. Yue, L.P. Song, Y.F. Fan, Z.X. Pan, P. Yang, Y. Ma, Q. Xu, B. Tang, Thiophene-containing covalent organic frameworks for overall photocatalytic H₂O₂ synthesis in water and seawater, *Angew. Chem. Int. Ed.* 62 (2023) 202309624.
- [34] Y. Liu, X. Wang, Y.J. Zhao, Q.Y. Wu, H.D. Nie, H.L. Si, H. Huang, Y. Liu, M. Shao, Z. H. Kang, Highly efficient metal-free catalyst from cellulose for hydrogen peroxide photoproduction instructed by machine learning and transient photovoltage technology, *Nano Res.* 15 (2022) 4000–4007.
- [35] H.B. Wang, M.L. Zhang, Y.R. Ma, B. Wang, H. Huang, Y. Liu, M.W. Shao, Z.H. Kang, Carbon dots derived from citric acid and glutathione as a highly efficient intracellular reactive oxygen species scavenger for alleviating the lipopolysaccharide-induced inflammation in macrophages, *ACS Appl. Mater. Interfaces* 12 (2020) 41088–41095.
- [36] X. Wang, Y. Ma, Q. Wu, Z.Z. Wang, Y.C. Tao, Y.J. Zhao, B. Wang, J.J. Cao, H. Wang, X.Q. Gu, H. Huang, S. Li, X.Y. Wang, F.R. Hu, M.W. Shao, L.S. Liao, T. K. Sham, Y. Liu, Z.H. Kang, Ultra-bright and stable pure blue light-emitting diode from O, N co-doped carbon dots, *Laser Photonics Rev.* 15 (2021) 2000412.
- [37] S. Li, B. Feng, X.X. Zhang, J. Tian, D. Wang, Y. Pei, M.H. Qiao, Y.F. Li, B.N. Zong, Multiple heteroatom-doped urea and thiourea-derived polymeric carbon nitride for high-performance visible light-driven photocatalytic O₂ reduction to H₂O₂, *Appl. Catal. B: Environ.* 335 (2023), 122879.
- [38] Y. Wu, J. Chen, H.N. Che, X. Gao, Y.H. Ao, P.F. Wang, Boosting 2e[−] oxygen reduction reaction in garland carbon nitride with carbon defects for high-efficient photocatalysis-self-Fenton degradation of 2,4-dichlorophenol, *Appl. Catal. B: Environ.* 307 (2022), 121185.
- [39] Y. Yang, G.G. Zeng, D.L. Huang, C. Zhang, D.H. He, C.Y. Zhou, W.J. Wang, W. P. Xiong, X.P. Li, B.S. Li, W.Y. Dong, Y. Zhou, Molecular engineering of polymeric carbon nitride for highly efficient photocatalytic oxytetracycline degradation and H₂O₂ production, *Appl. Catal. B: Environ.* 272 (2020), 118970.
- [40] Y. Guo, Q. Zhou, J. Nan, W. Shi, F. Cui, Y. Zhu, Perylenetetracarboxylic acid nanosheets with internal electric fields and anisotropic charge migration for photocatalytic hydrogen evolution, *Nat. Commun.* 13 (2022) 2067.
- [41] G.-h. Moon, M. Fujitsuka, S. Kim, T. Majima, X. Wang, W. Choi, Eco-friendly photochemical production of H₂O₂ through O₂ reduction over carbon nitride frameworks incorporated with multiple heteroelements, *ACS Catal.* 7 (2017) 2886–2895.
- [42] B.C. Moon, B. Bayarkhuu, K.A.I. Zhang, D.K. Lee, J. Byun, Solar-driven H₂O₂ production via cooperative auto- and photocatalytic oxidation in fine-tuned reaction media, *Energy Environ. Sci.* 15 (2022) 5082–5092.
- [43] Q.Y. Wu, J.J. Cao, X. Wang, Y. Liu, Y.J. Zhao, H. Wang, Y. Liu, H. Huang, F. Liao, M.W. Shao, Z.H. Kang, A metal-free photocatalyst for highly efficient hydrogen peroxide photoproduction in real seawater, *Nat. Commun.* 12 (2021) 483.
- [44] A.F. Zahrt, J.J. Henle, B.T. Rose, Y. Wang, W.T. Darrow, S.E. Denmark, Prediction of higher-selectivity catalysts by computer-driven workflow and machine learning, *Science* 363 (2019) 247.
- [45] J. Ohyama, T. Kinoshita, E. Funada, H. Yoshida, M. Machida, S. Nishimura, T. Uno, J. Fujima, I. Miyazato, L. Takahashi, K. Takahashi, Direct design of active catalysts for low temperature oxidative coupling of methane via machine learning and data mining, *Catal. Sci. Technol.* 11 (2021) 524–530.
- [46] M. Sun, A.W. Dougherty, B. Huang, Y. Li, C.H. Yan, Accelerating atomic catalyst discovery by theoretical calculations-machine learning strategy, *Adv. Energy Mater.* 10 (2020) 1903949.
- [47] N. Artrith, Z. Lin, J.G. Chen, Predicting the activity and selectivity of bimetallic metal catalysts for ethanol reforming using machine learning, *ACS Catal.* 10 (2020) 9438–9444.
- [48] M. Zhong, K. Tran, Y. Min, C. Wang, Z. Wang, C.-T. Dinh, P. De Luna, Z. Yu, A. S. Rasouli, P. Brodersen, S. Sun, O. Voznyy, C.-S. Tan, M. Askerka, F. Che, M. Liu, A. Seifitokaldani, Y. Pang, S.-C. Lo, A. Ip, Z. Ulissi, E.H. Sargent, Accelerated discovery of CO₂ electrocatalysts using active machine learning, *Nature* 581 (2020) 178–183.
- [49] Z.L. Wang, Y. Gu, L.X. Zheng, J.W. Hou, H.J. Zheng, S.J. Sun, L.Z. Wang, Machine learning guided dopant selection for metal oxide-based photoelectrochemical water splitting: the case study of Fe₂O₃ and CuO, *Adv. Mater.* 34 (2022) 202106776.
- [50] S.Z. Hu, X.Y. Qu, P. Li, F. Wang, Q. Li, L.J. Song, Y.F. Zhao, X.X. Kang, Photocatalytic oxygen reduction to hydrogen peroxide over copper doped graphitic carbon nitride hollow microsphere: The effect of Cu(I)-N active sites, *Chem. Eng. J.* 334 (2018) 410–418.